IEEE Access
Multidisciplinary ⋮ Rapid Review ⋮ Open Access Journal

Received June 20, 2020, accepted July 1, 2020, date of publication July 7, 2020, date of current version July 17, 2020.

Digital Object Identifier 10.1109/ACCESS.2020.3007707

Design and Dimensional Optimization of a Controllable Metamorphic Palletizing Robot

HUIQING CHEN[1,2,3], NINGQI ZHOU[1], AND RUGUI WANG[1,2], (Member, IEEE)

[1]College of Mechanical Engineering, Guangxi University, Nanning 530004, China
[2]College of Light Industry and Food Engineering, Guangxi University, Nanning 530004, China
[3]College of Mechanical and Control Engineering, Guilin University of Technology, Guilin 541004, China

Corresponding author: Rugui Wang (rugui@gxu.edu.cn)

This work was supported in part by the National Natural Science Foundation of China (NSFC) under Grant 51865001, and in part by the Major Special Fund for Science and Technology of Guangxi under Grant AA18118007-4.

ABSTRACT The controllable metamorphic mechanisms offer the advantages of adjustable mechanisms and multiple configurations. Most of these mechanisms are not yet applied in industry. To achieve the dimension calculation method for engineering applications as well as the effective and functional industrial prototype of these mechanisms, firstly, this paper designed a controllable metamorphic palletizing robot which can have 2-degrees-of-freedom (2-DOF) and single-DOF configurations. Further, this robot mechanism was studied using workspace analysis. The evaluation of its kinematic performance in workspace was presented. On this basis, a dimensional optimization method for metamorphic mechanisms based on workspace discretization was developed. The optimal workspace and corresponding dimensional parameters of this robot mechanism were obtained by this method and verified by the conventional calculation approach. A physical prototype of the robot was manufactured using optimized dimensional parameters and the feasibility as well as the practicality of its scheme was demonstrated.

INDEX TERMS Metamorphic mechanism, palletizing robot, dimensional optimization, workspace, singularity.

I. INTRODUCTION

The metamorphic mechanism was first proposed by Dai and Rees [1] at the 25th session of the ASME mechanism and robotics biennial conference in 1998 and has since received widespread attention from scholars around the world. Metamorphic mechanisms can realize mutual configurations and have therefore led to many notable achievements in design. From 2000 to 2003, some new metamorphic mechanisms such as the Ortho-planar mechanisms [2], the multiloop kinematotropic mechanisms [3], the metamorphic compliant ortho-planar mechanisms [4], and the metamorphic underwater vehicle [5] emerged successively. And they provided the initial references for the design of metamorphic mechanisms. Further to this, in 2008, Chen *et al*. [6] constructed a kind of special six-bar spherical metamorphic mechanism. In 2009, Dai *et al.* [7] presented a novel robotic hand by introducing a metamorphic palm that can generate reconfigurable motion. In 2010, Gan *et al*. [8] proposed a new metamorphic parallel mechanism that can change its mobility in a wide range. In 2013, they developed a new three-reconfigurable-translation-prismatic-spherical (3-rTPS) metamorphic parallel mechanism consisting of three reconfigurable rTPS limbs in perpendicular base planes [9]. Besides, Xu and Ding [10] designed the stride length of multi-legged robots based on metamorphic mechanism theory. More and more studies were focus on this flied in the past five years. For instance, in 2015, Wu *et al*. [11] carried out a configuration-switch mechanism for the three-universal-prismatic-universal (3-UPU) parallel mechanism. In 2016, Ye *et al*. [12] presented a family of metamorphic parallel mechanisms that can alter the performance of platform from full 6-DOF to 3-DOF. In 2017, Xu *et al*. [13] put forward a metamorphic mechanism cell which can realize deploying, self-locking, unlocking, retracting and interlocking with other cells. In 2018, Cui *et al*. [14] presented a newly metamorphic hand with a planar reconfigurable and flexible palm, which has advantage of dexterous and adaptable. And Wei and Dai [15] proposed group method for synthesis of

The associate editor coordinating the review of this manuscript and approving it for publication was Yan-Jun Liu.

metamorphic parallel mechanisms with the one-rotation-two-translation (1R2T) and two-rotation-one-translation (2R1T) reconfiguration. In addition, Jia *et al.* [16] designed a novel type of deployable grasping manipulator by using metamorphic principle. Then combined with the structural design of metamorphic mechanisms, [17] studied a mobile robot with high precision and high efficiency to fulfill people's demands. More recently, in 2019, Wang *et al.* [18] presented a novel plane-space polyhedral metamorphic mechanism. Following this, Song *et al.* [19] designed a novel 6R metamorphic mechanism by inserting two revolute joints to a Bennett mechanism.

In summary, a lot of achievements have been made in the design of metamorphic mechanisms, however, most of these mechanisms still stay in conceptual design, and have not been applied to specific practical industrial fields, especially in mechanical engineering, and have not yet become industrial robots in addition. Therefore, in order to achieve the industrial product design of metamorphic mechanisms and promote their wide application in industry, further researches on it are clearly needed.

The dimensional optimization is an effective way to ensure that the mechanisms can fit the requirements of the specific practical engineering. Then the rationality and the practicality of the design of mechanisms can be checked on this basis. To date, researches on the dimensional optimization of metamorphic mechanisms were carried out by Zhang *et al.* [20], [21], who proposed an optimization method for metamorphic mechanisms based on the principle of multidisciplinary design optimization. The optimization process was then created by constructing a two-level hierarchical scheme with a global optimizer and configuration optimizer loops. The optimization method in these references was focus on the working trajectory. However, it is not considered the practical engineering application of metamorphic mechanisms. Besides, no other references have investigated dimensional optimization of metamorphic mechanisms yet. Although scholars all over the world have achieved much in the optimization studies of conventional mechanisms such as multi-DOF mechanisms [22]–[27], robot mechanisms [28]–[36], and algorithms [37]–[39], dimensional optimization of metamorphic mechanisms is different from optimization of other traditional mechanisms because of the multiple configurations. There exist interrelations and differences among the optimization model of each configuration. Moreover, there are few references focusing on the optimization of metamorphic mechanisms in engineering application based on kinematics, workspace and dimensional parameters.

In view of the current status above, the contributions of this paper are as follow: The controllable metamorphic palletizing robot was designed based on the characteristics of metamorphic mechanisms and palletizing processes. The dimensional optimization method of metamorphic mechanisms based on workspace discretization was proposed. Using the dimensional parameters of the robot mechanism obtained by the proposed method, a prototype of this robot was manufactured, and the rationality of its design was validated. It provides references for dimensional optimization of metamorphic mechanisms for the practical engineering applications as well as for the design and manufacture of such mechanisms.

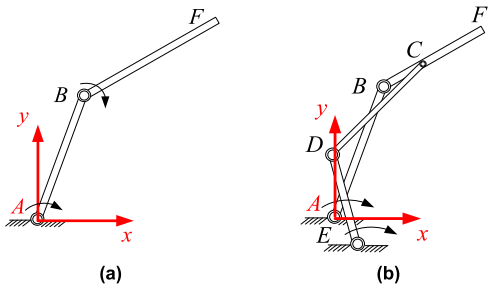

FIGURE 1. Planar branched chain: (a) Planar 2-DOF open-loop branched chain, (b) Mechanism with an additional branched chain.

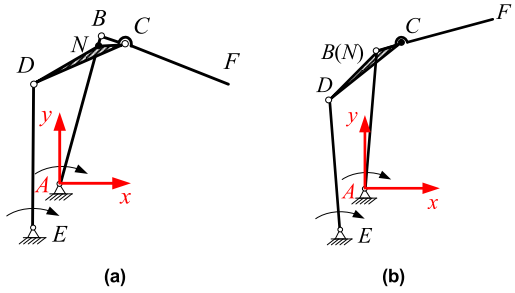

FIGURE 2. Diagrams of different mechanism configurations: (a) The 2-DOF configuration, (b) The single-DOF configuration.

II. DESIGN PROCESS OF ROBOT MECHANISM

A. DESIGN OF ROBOT MECHANISM

An open-loop branched chain, as shown in Fig. 1 (a), is the simplest way to realize positioning of a palletizing robot mechanism in a two-dimensional workspace. Consider installing the input motors of the palletizing robot mechanism on the frame and adding another branched chain (*E-D-C* branched chain), as shown in Fig. 1 (b). In this way, the entire branched chain structure becomes a closed-loop parallel branched chain. Although each of these mechanisms offers some advantages, only one configuration can be assembled. So it cannot have both advantages of these two mechanisms simultaneously in traditional way. In order to get more configurations, metamorphic mechanisms are introduced to solve this problem.

The configuration changing is realized by joint hinges separating and coinciding. As shown in Fig. 2, the triangular link *CND* is selected. When point *N* on the triangular link *CND* is separated from hinge *B* during the operating process, the mechanism is in the 2-DOF configuration, as shown in Fig. 2 (a). This can offer accurate positioning of output point *F* as a cargo is being grabbed and placed in another location. When point *N* coincides with

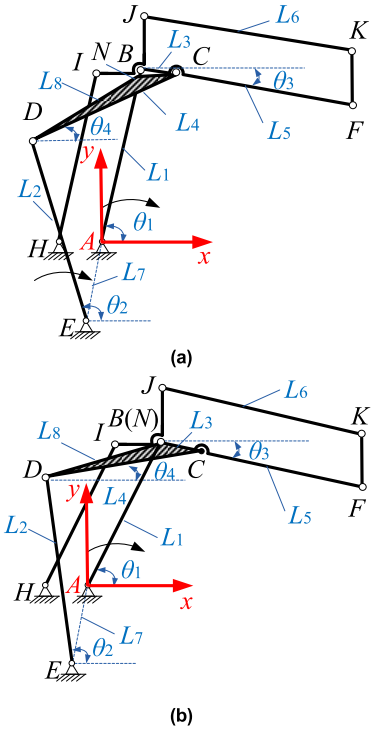

FIGURE 3. Diagrams of the mechanism: (a) The 2-DOF configuration, (b) The single-DOF configuration.

hinge B, the single-DOF configuration is selected. As shown in Fig. 2 (b), the mechanism can move rapidly in a large space and return quickly after the palletizing is completed, thereby realizing a single input. The robot is stable and easy to control.

The final design of the palletizing robot mechanism after adding the H-I-B-J-K-F branched chain is shown in Fig. 3. The following geometric relationships are satisfied: $L_{BI} = L_{AH}$, $L_{HI} = L_{AB}$, $L_{JK} = L_{BF}$, $L_{JB} = L_{KF}$. This ensures that the direction of output link KF remains unchanged while the robot mechanism is operating.

B. DESIGN OF ROBOT MODEL

The novel palletizing robot is design by Fig. 3. As shown in Fig. 4, hinges A and E, as well as the rotating frame, are driven by an input motor and speed reducer, and the output actuator is driven by the input motor.

To simplify the structure of metamorphic components, the clutch is installed at hinge C. The engagement and disengagement of the clutch at hinge C result in merging and separating of link BC and triangular link CND. Thus, it is convenient to realize automatically control. The DOF and the number of links of the robot are changing in different configurations. Therefore, this robot fits the concept of metamorphic mechanisms [1], [40], [41].

However, the dimensional parameters of the mechanism are unknown. This restricts the manufacture and application of the mechanism prototype. In view of this problem, a dimensional method of the mechanism is deduced in the following work.

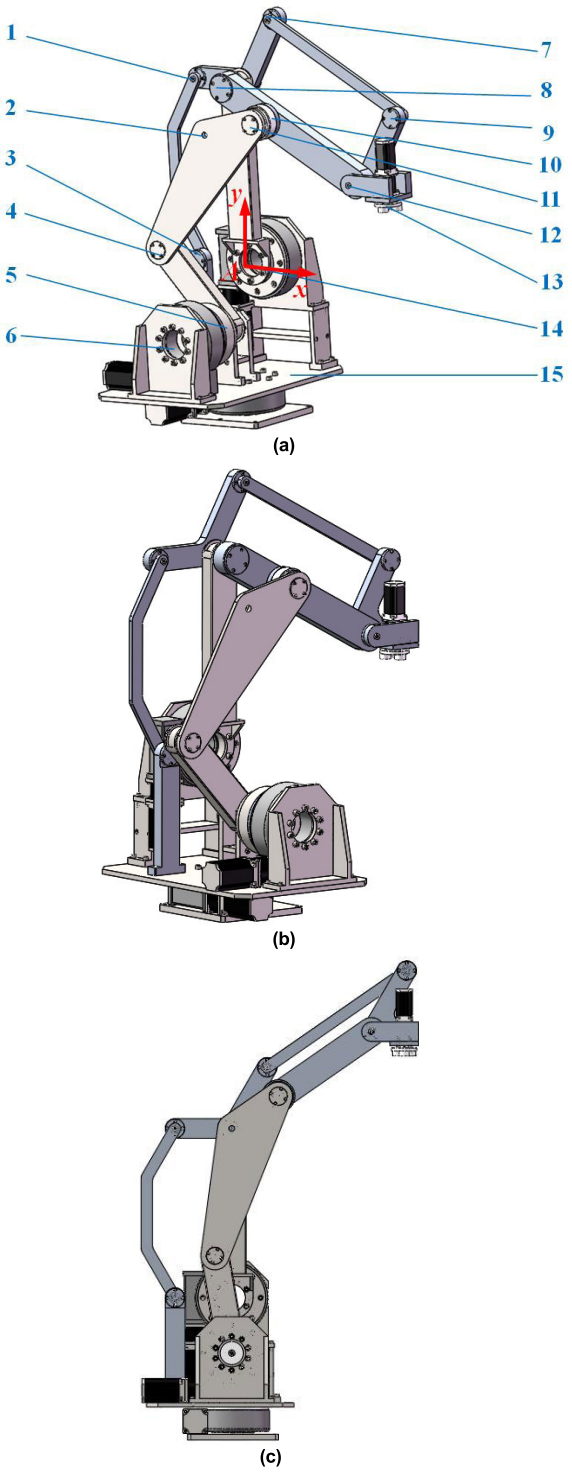

FIGURE 4. Structural view of palletizing robot prototype: (a) three-dimensional view I of a 2-DOF configuration, the numbers are marked as follow: 1, Hinge *I*; 2, *N* in triangular link *CND*; 3, Hinge *H*; 4, Hinge *D*; 5, point The clutch at the hinge *E*; 6, Hinge *E*; 7, Hinge *J*; 8, Hinge *B*; 9, Hinge *K*; 10, The clutch at the hinge *C*; 11, Hinge *C*; 12, Hinge *F*; 13, Output executor; 14, Hinge *A*; 15 Rotary frame. (b) three-dimensional view II of a 2-DOF configuration, (c) main view in a single-DOF configuration.

TABLE 1. Dimensional cases of 2-DOF configuration.

2-DOF configuration dimensional case	The dimensional relationships (where L_{max} is the length of the longest link; L_{min1} is the length of the shortest link; L_{min2} is the length of the second shortest link; L_a and L_b are the length of other two links, respectively.)	The type of the dimensional cases
1	$\begin{cases} L_{max}+L_{min1}+L_{min2} \le L_a+L_b \\ \begin{cases} L_{min1}=L_2 \\ L_{min2}=L_7 \end{cases} or \begin{cases} L_{min1}=L_7 \\ L_{min2}=L_2 \end{cases} \end{cases}$	An unconditional double crank mechanism
2	$\begin{cases} L_{max}+L_{min1}+L_{min2} \le L_a+L_b \\ \begin{cases} L_{min1}=L_3 \\ L_{min2}=L_7 \end{cases} or \begin{cases} L_{min1}=L_7 \\ L_{min2}=L_3 \end{cases} \end{cases}$	If rotating pairs A and E are turnover pairs, the mechanism is a conditional double crank mechanism; if one of these rotating pairs is not a turnover pair, the mechanism is a crank rocker mechanism.
3	$\begin{cases} L_{max}+L_{min1}+L_{min2} \le L_a+L_b \\ \begin{cases} L_{min1}=L_4 \\ L_{min2}=L_7 \end{cases} or \begin{cases} L_{min1}=L_7 \\ L_{min2}=L_4 \end{cases} \end{cases}$	If rotating pairs A and E are turnover pairs, the mechanism is a conditional double crank mechanism; if one of the rotating pairs A and E is not a turnover pair, the mechanism is a crank rocker mechanism.
4	$\begin{cases} L_{max}+L_{min1}+L_{min2} > L_a+L_b \\ L_{max}+L_{min2} \le L_a+L_b+L_{min1} \\ \begin{cases} L_{min1}=L_3 \, or \, L_4 \\ L_{min2} \ne L_4 \, or \, L_3 \end{cases} or \begin{cases} L_{min1} \ne L_4 \, or \, L_3 \\ L_{min2}=L_3 \, or \, L_4 \end{cases} or \begin{cases} L_{min1} \ne L_3 \, or \, L_4 \\ L_{min2} \ne L_4 \, or \, L_3 \end{cases} \end{cases}$	If rotating pairs A and E are turnover pairs, the mechanism is a conditional double crank mechanism; if one of the rotating pairs A and E is not a turnover pair, the mechanism is a crank rocker mechanism.
5	$\begin{cases} L_{max}+L_{min1}+L_{min2} > L_a+L_b \\ L_{max}+L_{min1} \le L_a+L_b+L_{min2} \\ L_{max}+L_{min2} \le L_a+L_b+L_{min1} \\ \begin{cases} L_{min1}=L_2 \\ L_{min2}=L_7 \end{cases} or \begin{cases} L_{min1}=L_7 \\ L_{min2}=L_2 \end{cases} \end{cases}$	A double crank mechanism.
6	$\begin{cases} L_{max}+L_{min1}+L_{min2} > L_a+L_b \\ \begin{cases} L_{min1}=L_3 \\ L_{min2}=L_4 \end{cases} or \begin{cases} L_{min1}=L_4 \\ L_{min2}=L_3 \end{cases} or \begin{cases} L_{max}+L_{min1} > L_a+L_b+L_{min2} \\ L_{max}+L_{min2} > L_a+L_b+L_{min1} \end{cases} \end{cases}$	A double rocker mechanism.

III. WORKSPACE ANALYSIS

A. DIMENSIONAL RELATIONSHIPS

Symbols denoting the lengths and angles of links in the robot mechanism are shown in Fig. 3. Coordinate values of points A, E, and F are marked as (x_A, y_A), (x_E, y_E), and (x_F, y_F), respectively.

To obtain the smallest robot base structure possible, the following settings were used: L_1 is not the length of one of the two shortest links; L_7 is not the length of the longest link. According to [42], [43], dimensional cases of 2-DOF and single-DOF configuration can be classified in Table 1 and 2, respectively.

B. SINGULARITY ANALYSIS

As shown in Fig. 3, displacements of output point F of the workspace in the x and y directions can be expressed as follows:

$$\begin{cases} x_F = x_A + L_1\cos\theta_1 + L_6\cos\theta_3 \\ y_F = y_A + L_1\sin\theta_1 + L_6\sin\theta_3 \end{cases} \tag{1}$$

The relationship of $\theta_1, \theta_2, \theta_3$ and θ_4 are given in the Appendix.

Taking the derivative of (1) with respect to time t:

$$\begin{cases} 2-\text{DOF configuration}: \\ \begin{bmatrix} \frac{dx_F}{dt} \\ \frac{dy_F}{dt} \end{bmatrix} = \begin{bmatrix} \frac{\partial x_F}{\partial \theta_1^{(1)}} & \frac{\partial x_F}{\partial \theta_2^{(1)}} \\ \frac{\partial y_F}{\partial \theta_1^{(1)}} & \frac{\partial y_F}{\partial \theta_2^{(1)}} \end{bmatrix} \begin{bmatrix} \frac{d\theta_1^{(1)}}{dt} \\ \frac{d\theta_2^{(1)}}{dt} \end{bmatrix} = \boldsymbol{J}_1 \begin{bmatrix} \frac{d\theta_1^{(1)}}{dt} \\ \frac{d\theta_2^{(1)}}{dt} \end{bmatrix} \\ \text{Single}-\text{DOF configuration}: \\ \begin{bmatrix} \frac{dx_F}{dt} \\ \frac{dy_F}{dt} \end{bmatrix} = \begin{bmatrix} \frac{\partial x_F}{\partial \theta_1^{(2)}} \frac{\partial \theta_1^{(2)}}{\partial \phi} \\ \frac{\partial y_F}{\partial \theta_1^{(2)}} \frac{\partial \theta_1^{(2)}}{\partial \phi} \end{bmatrix} \frac{d\phi}{dt} = \boldsymbol{J}_2 \frac{d\phi}{dt} \end{cases} \tag{2}$$

where the numeric superscripts (1) and (2) denote the 2-DOF and the single-DOF configuration, respectively. $\boldsymbol{J}_1$ and $\boldsymbol{J}_2$ are jacobian matrices of the 2-DOF configuration and the single-DOF configuration, respectively. Furthermore, the singular values $\sigma^{(\xi)}$ $(\xi = 1, 2)$ of $\boldsymbol{J}_1$ and $\boldsymbol{J}_2$ can be derived using the singular value decomposition method.

The mechanism should not span the singular positions, $\theta_1 \in (0, \pi)$ and $\theta_2 \in (0, \pi)$ are satisfied. Thus, in 2-DOF

TABLE 2. Dimensional cases of single-DOF configuration.

Single-DOF configuration dimensional case	The dimensional relationships (the definition of L_{max} , L_{min1} , L_a and L_b are the same as Table 1.)	The type of the dimensional cases
1	$\begin{cases} L_{max}+L_{min1} \le L_a+L_b \\ L_{min1}=L_7 \end{cases}$	A double crank mechanism
2	$\begin{cases} L_{max}+L_{min1} \le L_a+L_b \\ L_{min1}=L_2 \end{cases}$	A crank rocker mechanism
3	$\begin{cases} L_{max}+L_{min1} \le L_a+L_b \\ L_{min1}=L_8 \end{cases}$	A double rocker mechanism.

configuration, only one or none of the singular positions, $\theta_3^{(1)}=\theta_1^{(1)}$ or $\theta_3^{(1)}=\theta_1^{(1)}+\pi$, will occur. Similarly, $\theta_4^{(1)}=\theta_2^{(1)}$ or $\theta_4^{(1)}=\theta_2^{(1)}+\pi$, $\theta_4^{(1)}=\theta_3^{(1)}$ or $\theta_4^{(1)}=\theta_3^{(1)}+\pi$ are the same as above. $\theta_1^{(1)}$ is known, the singular positions are analyzed as follows [44]:

1) Singular positions of $\theta_3^{(1)}=\theta_1^{(1)}$ and $\theta_3^{(1)}=\theta_1^{(1)}+\pi$: $\theta_2^{(1)}$ and $\theta_3^{(1)}$ are deduced based on $\theta_1^{(1)}$.

2) Singular positions of $\theta_4^{(1)}=\theta_2^{(1)}$ and $\theta_4^{(1)}=\theta_2^{(1)}+\pi$:

$$\begin{cases} \theta_1^{(1)}=\begin{cases} \pi-\phi+\gamma & (x_E<x_A)\cup[(x_E=x_A)\cap(y_E<y_A)] \\ \phi+\gamma & (x_E>x_A)\cup[(x_E=x_A)\cap(y_E>y_A)] \end{cases} \\ \theta_3^{(1)}=\begin{cases} \pi-\nu_{12}+\gamma & (x_E<x_A)\cup[(x_E=x_A)\cap(y_E<y_A)] \\ \nu_{12}+\gamma & (x_E>x_A)\cup[(x_E=x_A)\cap(y_E>y_A)] \end{cases} \\ \theta_2^{(1)}=\begin{cases} \pi-\kappa_{12}+\gamma & (x_E<x_A)\cup[(x_E=x_A)\cap(y_E<y_A)] \\ \kappa_{12}+\gamma & (x_E>x_A)\cup[(x_E=x_A)\cap(y_E>y_A)] \end{cases} \end{cases} \tag{3}$$

where ν_{12} and κ_{12} in (3) are given in the Appendix.

3) Singular positions of $\theta_4^{(1)}=\theta_3^{(1)}$ and $\theta_4^{(1)}=\theta_3^{(1)}+\pi$:

$$\begin{cases} \theta_1^{(1)}=\begin{cases} \pi-\phi+\gamma & (x_E<x_A)\cup[(x_E=x_A)\cap(y_E<y_A)] \\ \phi+\gamma & (x_E>x_A)\cup[(x_E=x_A)\cap(y_E>y_A)] \end{cases} \\ \theta_3^{(1)}=\begin{cases} \pi-\nu_{22}+\gamma & (x_E<x_A)\cup[(x_E=x_A)\cap(y_E<y_A)] \\ \nu_{22}+\gamma & (x_E>x_A)\cup[(x_E=x_A)\cap(y_E>y_A)] \end{cases} \\ \theta_2^{(1)}=\begin{cases} \pi-\kappa_{22}+\gamma & (x_E<x_A)\cup[(x_E=x_A)\cap(y_E<y_A)] \\ \kappa_{22}+\gamma & (x_E>x_A)\cup[(x_E=x_A)\cap(y_E>y_A)] \end{cases} \end{cases} \tag{4}$$

where ν_{22} and κ_{22} in (4) are given in the Appendix.

Then, the trajectory of F in these singular positions can be solved by (1) according to geometry.

C. WORKSPACE OF THE BRANCHED CHAINS

The workspace of the *A*-*B*-*F* branched chain is shown as the yellow area in Fig.5. The circular workspace satisfies the following condition:

$$|L_1-L_6| \le L_{AF} \le |L_1+L_6| \tag{5}$$

Since θ_1 must be within a reasonable range of $\theta_1 \in (0,\pi)$ and the workspace is symmetrical after the rotating motor is installed on the frame, the effective workspace that the *A*-*B*-*F* branched chain can achieve is shown as the yellow area of Fig. 6, called the theoretical workspace. After adding *E*-*D*-*C* branched chain, since θ_2 must satisfy a reasonable range of $\theta_2 \in (0,\pi)$, the suitable workspace is shown as the yellow area of Fig. 7. Gray areas indicate that $\theta_2<0$ and$\theta_2>\pi$ are invalid areas, in which only one of them appears.

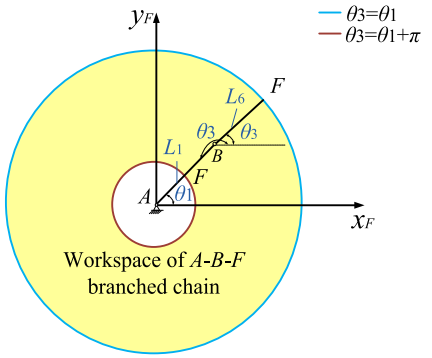

FIGURE 5. Workspace of *A*-*B*-*F* branched chain.

When $\theta_2=0$ or π, then:

$$\begin{cases} \theta_1^{(1)}=\begin{cases} \pi-\phi+\delta & (x_E<x_A)\cup[(x_E=x_A)\cap(y_E<y_A)] \\ \phi+\delta & (x_E>x_A)\cup[(x_E=x_A)\cap(y_E>y_A)] \end{cases} \\ \theta_3^{(1)}=\begin{cases} \pi-\nu_{23}+\delta & (x_E<x_A)\cup[(x_E=x_A)\cap(y_E<y_A)] \\ \nu_{23}+\delta & (x_E>x_A)\cup[(x_E=x_A)\cap(y_E>y_A)] \end{cases} \\ \theta_4^{(1)}=\begin{cases} \pi-\kappa_{23}+\delta & (x_E<x_A)\cup[(x_E=x_A)\cap(y_E<y_A)] \\ \kappa_{23}+\delta & (x_E>x_A)\cup[(x_E=x_A)\cap(y_E>y_A)] \end{cases} \end{cases} \tag{6}$$

where ν_{23}, κ_{23}, and δ in (6) are given in the Appendix. For this condition, the trajectory of F can be solved by (1).

D. THE EVALUATION OF THE MECHANISM KINEMATIC PEFORMANCE IN WORKSPACE

In single-DOF configuration, when the assembly conditions formed by singular positions are not satisfied, the singular positions do not occur. The singular positions of each case are shown in Table 3. From (1), (3), (4) and (6), a valid workspace for the 2-DOF configuration dimensional cases 1–6 is shown

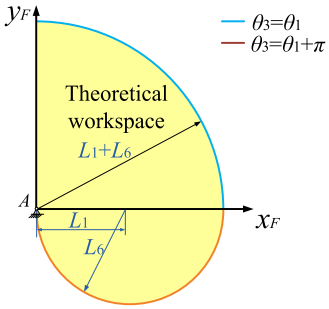

FIGURE 6. Theoretical workspace.

TABLE 3. The singular positions.

Configuration	Case	The singular positions
2-DOF	1	Either $\theta_4^{(1)}=\theta_2^{(1)}$ or $\theta_4^{(1)}=\theta_2^{(1)}+\pi$ exists.
2-DOF	2	Either $\theta_3^{(1)}=\theta_1^{(1)}$ or $\theta_3^{(1)}=\theta_1^{(1)}+\pi$ exists; Either $\theta_4^{(1)}=\theta_3^{(1)}$ or $\theta_4^{(1)}=\theta_3^{(1)}+\pi$ exists.
2-DOF	3	Either $\theta_4^{(1)}=\theta_2^{(1)}$ or $\theta_4^{(1)}=\theta_2^{(1)}+\pi$ may exist.
		Either $\theta_4^{(1)}=\theta_2^{(1)}$ or $\theta_4^{(1)}=\theta_2^{(1)}+\pi$ may exist;
2-DOF	4,5,6	Either $\theta_3^{(1)}=\theta_1^{(1)}$ or $\theta_3^{(1)}=\theta_1^{(1)}+\pi$ may exist;
		Either $\theta_4^{(1)}=\theta_3^{(1)}$ or $\theta_4^{(1)}=\theta_3^{(1)}+\pi$ may exist.
Single-DOF	1	None.
Single-DOF	2,3	The dead points.

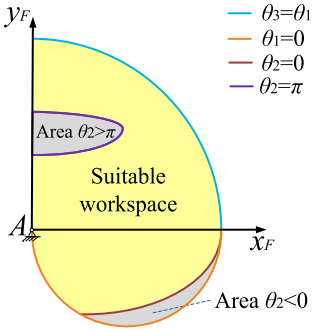

FIGURE 7. Suitable workspace area after adding *E-D-C* branched chain.

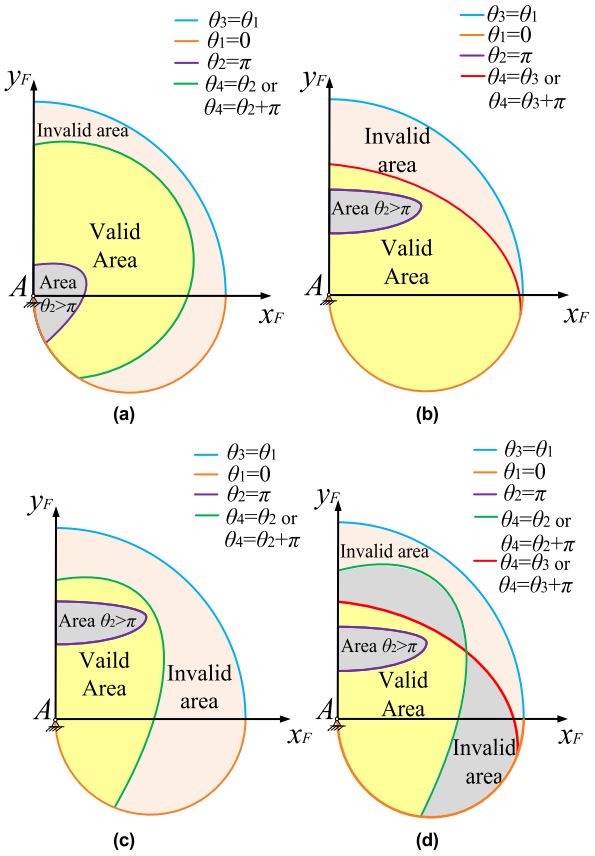

FIGURE 8. Valid workspaces for each dimensional case of the 2-DOF configuration: (a) Case 1, (b) Case 2, (c) Case 3, (d) Cases 4–6.

in Fig. 8, indicated by the area in yellow. The gray and light orange color denotes invalid areas.

In general, the workspace, condition number ($\sigma_{\max}^{(\xi)}/\sigma_{\min}^{(\xi)}$) [45], minimum singular value ($\sigma_{\min}^{(\xi)}$), and manipulability ($\sigma_1^{(\xi)}\sigma_2^{(\xi)}\cdots\sigma_n^{(\xi)}$) [46] are used to evaluate kinematic performance in a mechanism's workspace. From (1) and (2), when the mechanism is close to the singular positions $\theta_3^{(1)}=\theta_1^{(1)}$, $\theta_1^{(1)}=\theta_3^{(1)}+\pi$, $\theta_4^{(1)}=\theta_2^{(1)}$ and $\theta_4^{(1)}=\theta_2^{(1)}+\pi$ in the 2-DOF configuration, $\sigma_{\min}^{(1)}=0$. When the mechanism is close to singular positions $\theta_4^{(1)}=\theta_3^{(1)}$ and $\theta_4^{(1)}=\theta_3^{(1)}+\pi$, then $\sigma_{\max}^{(1)}=\infty$ and $\sigma_{\min}^{(1)}$ does not tend to infinity. In the single-DOF configuration, when the mechanism is in the singular position, $\sigma_{\min}^{(2)}=0$ and $\sigma_{\max}^{(2)}$ is not close to zero. Therefore, the reciprocal of the condition number $k_J^{(\xi)}$ is selected as the evaluation index of kinematic performance in the workspace:

$$k_J^{(\xi)}=\sigma_{\min}^{(\xi)}\Big/\sigma_{\max}^{(\xi)} \tag{7}$$

where $k_J^{(\xi)}\in[0,1]$. When $k_J^{(\xi)}$ is small, kinematic performance of the mechanism is poor; when $k_J^{(\xi)}$ is lager, kinematics performance of the mechanism is good; when $k_J^{(\xi)}=0$, the mechanism is in the singular position.

In certain situations, $\sigma_{\min}^{(\xi)}$ and $\sigma_{\max}^{(\xi)}$ may be close to zero, but $k_J^{(\xi)}$ is large. However, since $\sigma_{\min}^{(\xi)}$ is small, kinematic performance of the mechanism is poor. Therefore, the condition number and minimum singular value should be comprehensively considered. The following assumptions are made: $k_J^{(\xi)}$ is valid in area $\sigma_{\min}^{(\xi)}\geq\bar{\sigma}_{\min}^{(\xi)}$ ($\bar{\sigma}_{\min}^{(\xi)}$ is the minimum allowable value of $\sigma^{(\xi)}$), area $\sigma_{\min}^{(\xi)}<\bar{\sigma}_{\min}^{(\xi)}$ is invalid. Finally, the area with singular value $k_J^{(1)}\geq\bar{k}_{J\min}^{(1)}$ ($\bar{k}_{J\min}^{(\xi)}$ is the minimum allowable value of $k_J^{(\xi)}$) under the condition $\sigma_{\min}^{(1)}\geq\bar{\sigma}_{\min}^{(1)}$ is selected as the suitable workspace area, as shown in Fig. 9.

In single-DOF configuration, the workspace is a curve, as shown in Fig. 10. Singular values $\sigma^{(2)}$ corresponding to positions of the point F along the trajectory under this

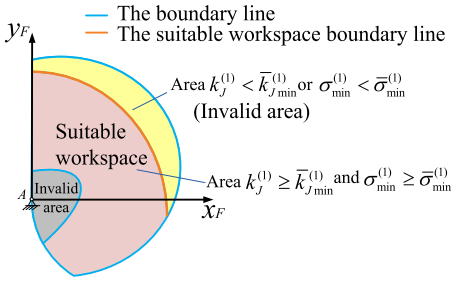

FIGURE 9. Suitable workspace area.

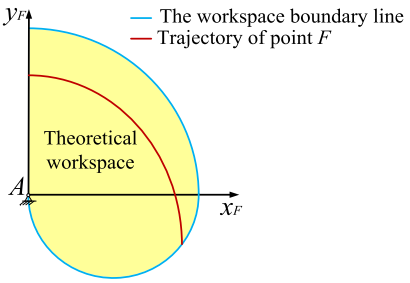

FIGURE 10. Trajectory of point *F* in the single-DOF configuration.

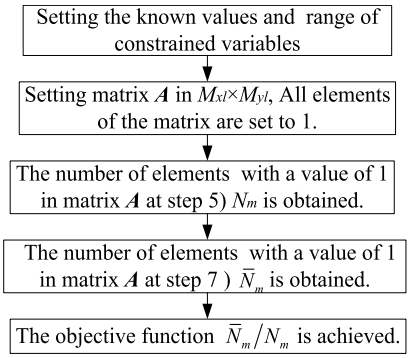

FIGURE 11. The calculation process of the objective function.

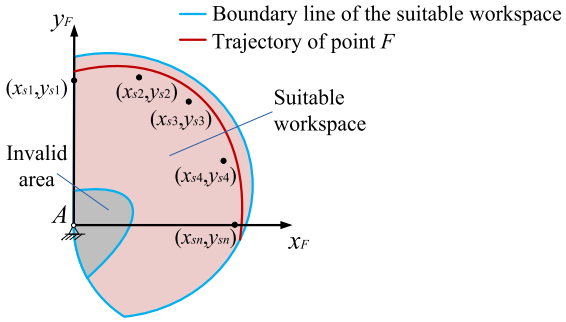

FIGURE 12. Workspace constraints for the single-DOF configuration.

configuration can be determined by (2). In addition, $k_J^{(2)}$ can be determined by (7). The edges of the suitable workspace of the 2-DOF configuration are often selected and $k_J^{(2)} \geq \bar{k}_{J\min}^{(2)}$ must be satisfied.

IV. DIMENSIONAL OPTIMAZATION METHOD BASED ON WORKSPACE DISCRETIZATION

Since the workspace of the single-DOF configuration is contained in the workspace of the 2-DOF configuration, the following optimization strategy is proposed: First, the suitable workspace and corresponding preliminary dimensional parameters of the 2-DOF configuration are optimized according to the dimensional parameters of the 2-DOF configuration dimensional cases 1–6. Workspace restrictions of the single-DOF configuration were then used as constraints to further optimize the workspace of the 2-DOF configuration.

The lengths L_1 and L_6 are known values; lengths L_2, L_3, L_4, x_E, and y_E are taken as optimization variables. Finally, L_8 is determined according to the constraints of the single-DOF configuration workspace.

To obtain the maximum workspace of the mechanism under the limitation of the dimensional parameters, the ratio of suitable workspace area $\bar{S}$ of the 2-DOF configuration to theoretical workspace area S is chosen as the objective function. However, $\bar{S}$ is difficult to solve. Therefore, the continuous workspace is replaced by a sufficient number of discrete points for the optimization calculations. To improve the operational efficiency, discrete points with large distances can be selected first. When the optimization is complete, discrete points with smaller distance are re-selected to verify the results. The objective function is the ratio of the number of discrete points $\bar{N}_m$ in the suitable workspace area $\bar{S}$ of the 2-DOF configuration to the number of discrete points N_m in the theoretical workspace area S, $\bar{N}_m / N_m$.

The steps of the dimensional optimization calculation are as follows:

1) Define L_1 and L_6 according to the task requirements.

2) The range of constrained variables L_2, L_3, L_4, x_E, and y_E are determined according to the dimensional requirements of the prototype. Constrained variables are generated using the optimization algorithm in this range.

3) Length constraints for the 2-DOF configuration dimensional cases 1–6 are obtained.

4) The interval between discrete points with larger distances is d_l. Setting matrix $\boldsymbol{A}$ to express the workspace, its order is $M_{xl} \times M_{yl}$. Where $M_{xl} = (L_1 + L_6)/d_l + 1$, $M_{yl} = (L_1 + L_6 + L_6)/d_l + 1$. All elements of the matrix are set to 1 and the matrix is referred to as the valid discrete point matrix in the workspace.

5) Generate an array of angles according to the size interval $\pi \times 10^{-5}$. Then, substituting $\theta_1 = 0$ and $\theta_1 = \theta_3$ into (1), a series of trajectory points x_{F1}, y_{F1}, x_{F2}, y_{F2},..., x_{Fn_1}, y_{Fn_1} can be obtained. Coordinates of all trajectory points are processed using $x_{Fi}/d_l + 1$ and $y_{Fi}/d_l + 1$ $(i = 1, 2, \ldots, n_1)$. A rounding operation is then performed and a series of integers (M_{xF}, M_{yF}) are obtained. The element of the M_{xFi}th row and the M_{yFi}th column of the matrix $\boldsymbol{A}$ is denoted as $\boldsymbol{A}(M_{xFi}, M_{yFi})$. Setting $\boldsymbol{A}(M_{xFi}, M_{yFi}) = 0$, points on the trajectory are stored in matrix $\boldsymbol{A}$ when $\theta_1 = 0$ and $\theta_1 = \theta_3$. The elements are zero in the outer region of $\boldsymbol{A}(M_{xFj}, M_{yFj})$

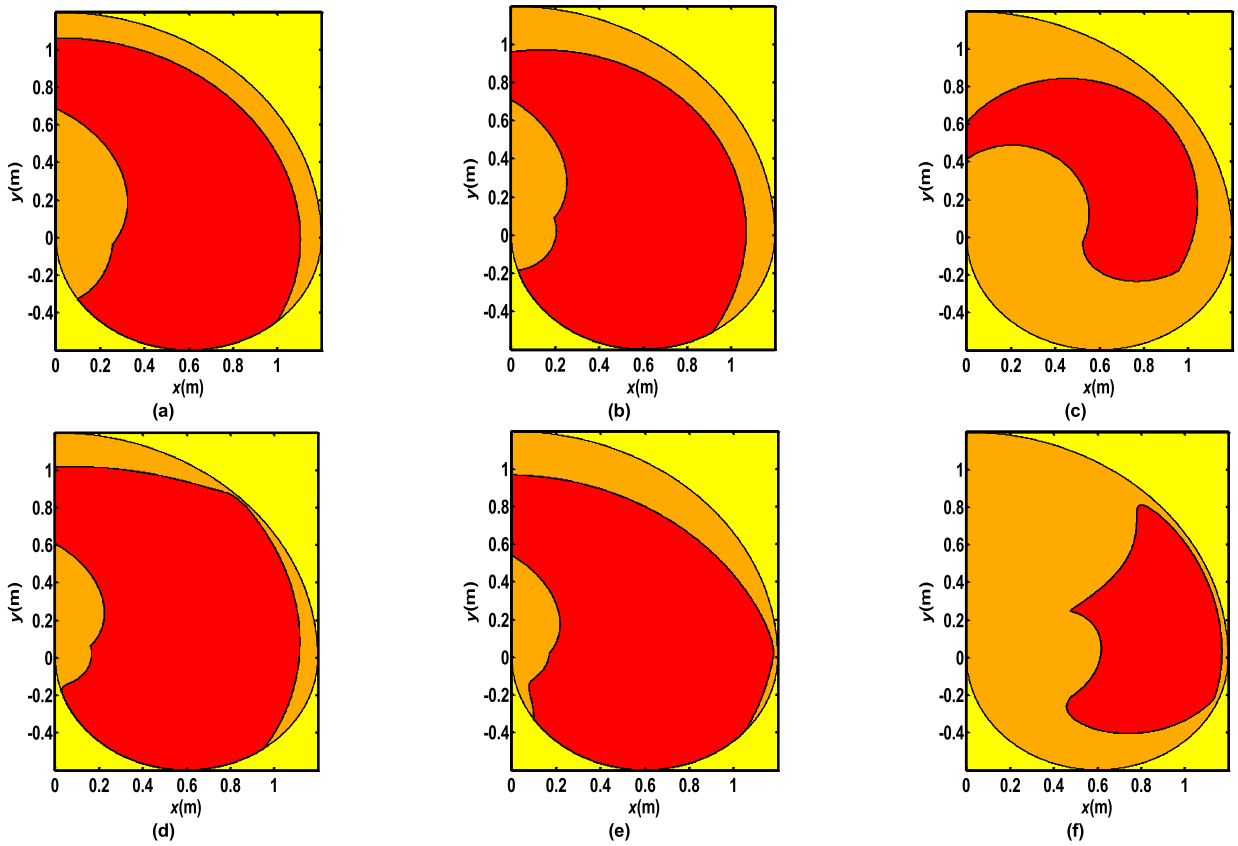

FIGURE 13. Suitable workspaces for each dimensional case of the 2-DOF configuration: (a) Case 1, (b) Case 2, (c) Case 3, (d) Case 4, (e) Case 5, (f) Case 6.

(lower lateral range of $\theta_3 \in (-\pi, 0)$ in position $\theta_1 = 0$, upper lateral range of $\theta_1 \in (0, \pi/2)$ in the position curve $\theta_1 = \theta_3$), Then the number of elements N_m with a value of 1 in matrix $\boldsymbol{A}$ is determined.

6) Furthermore, a series of trajectory points x_{Fj}, y_{Fj} ($j = 1, 2, \ldots, n_2$) about $\theta_2 = \pi$, $\theta_2 = \theta_4$ and $\theta_3 = \theta_4$ are obtained from (1), (3), (4) and (6). Coordinates of all trajectory points are processed using $x_{Fj}/d_l + 1$ and $y_{Fj}/d_l + 1$. A round operation is performed and a series of integers $M_{x_{Fj}}$, $M_{y_{Fj}}$ is obtained. Set $\boldsymbol{A}(M_{x_{Fj}},\ M_{y_{Fj}}) = 0$. Points of the trajectory points are stored in matrix $\boldsymbol{A}$ when $\theta_2 = \pi$, $\theta_2 = \theta_4$ and $\theta_3 = \theta_4$. Elements in the outer region of $\boldsymbol{A}(M_{x_{Fj}},\ M_{y_{Fj}})$ are zero (in ranges $\theta_2 > \pi$, $\theta_2 < \theta_4$ and $\theta_4 < \theta_3$).

7) Coordinate values (x_F, y_F) corresponding to elements of $\boldsymbol{A}(M_{x_F},\ M_{y_F})$ with a value of 1 in matrix $\boldsymbol{A}$ are inversely calculated. $k_J^{(1)}$ corresponding to coordinate values are obtained from (1), (2) and (7). All elements of matrix $\boldsymbol{A}$ corresponding to $k_J^{(1)} < \bar{k}_{J\min}^{(1)}$ or $\sigma_{\min}^{(1)} < \bar{\sigma}_{\min}^{(1)}$ are set to zero. Regions formed by elements with a value of 1 in matrix $\boldsymbol{A}$ are suitable workspace regions, and the number of elements with a value of 1 in matrix $\boldsymbol{A}$ is $\bar{N}_m$.

8) The calculation process of the objective function is shown in Fig. 11. The maximum value of the objective function $\bar{N}_m/N_m$ is obtained by repeating the optimization calculation. Interval $d_{l\,\min}$ between discrete points with smaller distances is assessed as in steps 4)–7). If the optimized variables not satisfy all various constraints, the optimization of step 2) is carried out again to ensure the results are accurate.

9) Based on optimization results for the 2-DOF configuration dimensional cases 1–6, improved optimization results of the suitable workspace area are selected. To increase the range of the trajectory of the single-DOF configuration, it must be in the upper range of the set of coordinate values (x_1, y_1), $(x_2, y_2), \ldots, (x_n, y_n)$ and satisfy the constraint condition $k_J^{(2)} \geq \bar{k}_{J\min}^{(2)}$, as shown in Fig.12. The optimization variables are still the same and $\bar{N}_m/N_m$ is the objective function to be optimized again.

10) Optimization results are obtained and assessed. If the results are not suitable, we must return to step 9) or step 1) to re-optimize. Otherwise, suitable workspace and coupling dimensional parameters have been obtained.

11) A smaller interval $d_{l\,\min}$ used to assess whether the optimized variables satisfy all of the various constraints according to steps 4)–7). Otherwise, return to step 1) to re-calculate to ensure the results are accurate.

V. CASE STUDY

According to the task requirements, $L_1 = L_6 = 0.6$ m is selected. Considering the manufacturing constraints and the priority for making the robot prototype compact, the con-

TABLE 4. Optimization results.

2-DOF configuration	Optimized variables (m)					Objective function
Dimensional case	L_2	L_4	L_3	x_E	y_E	$\bar{N}_m/N_m$
1	0.32013	0.60720	0.36817	-0.00108	-0.03952	0.744133
2	0.34621	0.58123	0.24908	-0.02713	-0.07335	0.725587
3	0.59968	0.27089	0.47604	0.14045	0.14710	0.380394
4	0.33160	0.60572	0.23273	0.08501	-0.18009	0.791446
5	0.35603	0.62642	0.35679	0.01396	-0.18327	0.755110
6	0.52673	0.26241	0.25786	0.19926	0.17358	0.335102

TABLE 5. Calculation results for smaller distances.

2-DOF configuration	Optimized variables (m)					Objective function
Dimensional case	L_2	L_4	L_3	x_E	y_E	$\bar{N}_m/N_m$
1	0.320	0.607	0.368	-0.001	-0.040	0.7236
2	0.346	0.581	0.249	-0.027	-0.073	0.7082
3	0.600	0.271	0.476	0.140	0.147	0.3676
4	0.332	0.606	0.233	0.085	-0.180	0.8209
5	0.356	0.626	0.357	0.014	-0.183	0.7663
6	0.527	0.262	0.258	0.199	0.174	0.3259

TABLE 6. Re-optimization results.

2-DOF configuration	Optimized variables (m)					Objective function	The area range of $\theta_2 > \pi$ (m)
Dimensional case	L_2	L_4	L_3	x_E	y_E	$\bar{N}_m/N_m$	in x direction
1					No solution		
2					No solution		
4	0.350	0.608	0.200	0	-0.196	0.8476	[0, 0.1775]
5	0.278	0.656	0.278	-0.017	-0.119	0.7645	[0, 0.3325]

TABLE 7. The maximum calculation results (The spacing of each optimized variable is 0.02 m).

The corresponding range of discrete values of optimized variables (m)					The maximum average of objective function
L_2	L_4	L_3	x_E	y_E	$\bar{N}_m/N_m$
[0.34,0.36]	[0.60,0.62]	[0.20,0.22]	[-0.02,0.00]	[-0.20,-0.18]	0.8403

ditions restricting the lengths of the links are selected as follows:

$$\begin{cases} \text{Find } \{L_2, L_3, L_4, x_E, y_E\} \\ \text{Max} \quad \bar{N}_m/N_m \\ \text{s.t.} \\ L_2 \in [0.12\text{ m}, 0.6\text{ m}] \\ L_3 \in [0.2\text{ m}, 0.48\text{ m}] \\ L_4 \in [0.12\text{ m}, 0.9\text{ m}] \\ x_E \in [-0.2\text{ m}, 0.2\text{ m}] \\ y_E \in [-0.2\text{ m}, 0.2\text{ m}] \end{cases} \tag{8}$$

To avoid excessive input torque due to the singular position of the prototype, set $\bar{k}_{J\min}^{(1)} = 0.1$, $\bar{\sigma}_{\min}^{(1)} = 0.15$, and $\bar{k}_{J\min}^{(2)} = 0.35$.

Taking intervals between discrete points with larger distance in workspace as 0.025 m, the genetic algorithm was used to optimize the calculation. Optimization results are presented in Table 4. The optimization variables were substituted into the workspace for a smaller distance of 0.0025 m. The calculation results are presented in Table 5 and the workspace is shown in Fig. 13. Red areas represent the suitable workspace area $\bar{S}(k_J^{(1)} \geq \bar{k}_{J\min}^{(1)}$ and $\sigma_{\min}^{(1)} \geq \bar{\sigma}_{\min}^{(1)})$

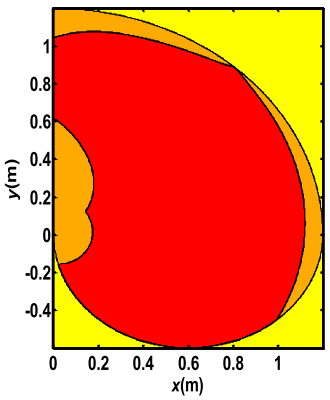

FIGURE 14. Re-optimized workspace.

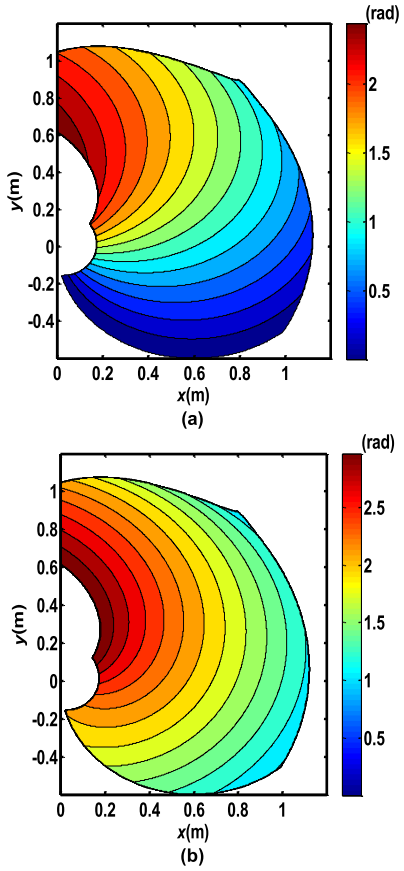

FIGURE 15. Contours of the input angle of the mechanism after re-optimization: (a) θ_1, (b) θ_2.

for the mechanism. Dark yellow indicates the areas where $k_J^{(1)} < \bar{k}_{J\min}^{(1)}$ or $\sigma_{\min}^{(1)} < \bar{\sigma}_{\min}^{(1)}$ and unavailable areas. The theoretical workspace area is the red areas plus dark yellow areas. The yellow areas are outside the theoretical workspace.

The results in Table 5 show that the suitable workspaces of 2-DOF configuration dimensional cases 1, 2, 4 and 5 are far larger than the dimensional cases 3 and 6. The suitable workspaces of the former cases are close to each other and they are selected for further optimization. The 2-DOF configuration dimensional case 1 is an unconditional double crank mechanism, and cases 2, 4, and 5 are conditional double crank mechanisms [43].

The trajectory of the single-DOF configuration workspace constraint condition is set above a series of coordinate points (0.2 m,1 m), (0.4 m,0.97 m), (0.6 m,0.85 m), (0.8 m,0.7 m), and (1 m,0 m). To design a suitable workspace free from interference between links, $x_E \leq 0$ must be satisfied. The optimum conditions are as follows:

$$\begin{cases} L_2 \in [0.12\text{ m}, 0.36\text{ m}] \\ L_3 \in [0.2\text{ m}, 0.3\text{ m}] \\ L_4 \in [0.12\text{ m}, 0.9\text{ m}] \\ x_E \in [-0.1\text{ m}, 0\text{ m}] \\ y_E \in [-0.2\text{ m}, 0\text{ m}] \end{cases}$$

And other constraints remain unchanged.

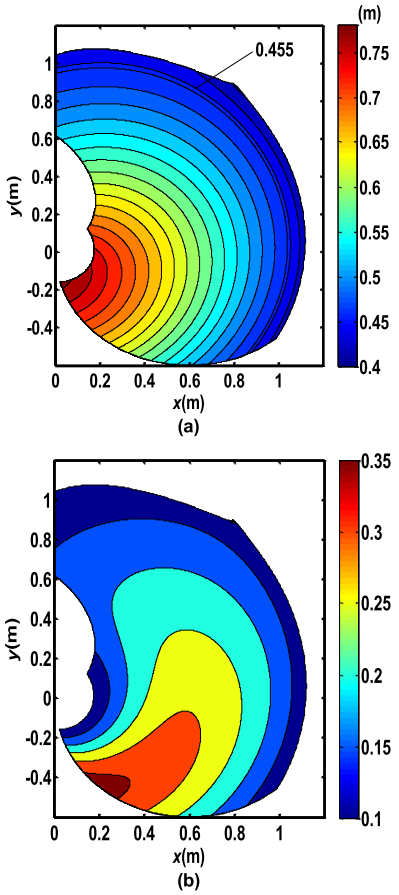

FIGURE 16. Contour of (a) distance distribution between points B and N in mechanism workspace after re-optimization, of (b) $k_J^{(1)}$ distribution in suitable workspace after re-optimization.

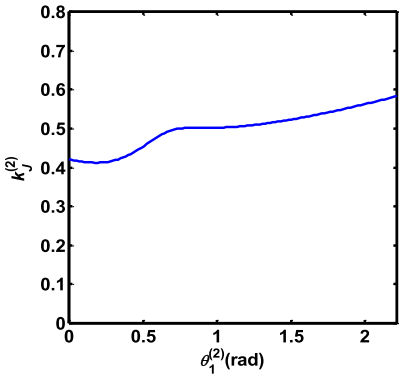

FIGURE 17. Correspondence diagram of $k_J^{(2)}$ and $\theta_1^{(2)}$.

Results of the further optimization are shown in Table 6. Both objective functions of cases 1 and 2 are no solution. The suitable workspace of case 4 is larger than case 5. The area range of $\theta_2 > \pi$ of the former in x direction is smaller than which of the latter. Thus the former is selected as the optimized dimension of this mechanism.

The conventional calculation approach that all the ranges of optimized variables are dispersed by the appropriate

FIGURE 18. Structural views of the physical prototype: (a) The initial position, the numbers are marked as follow: 1, the clutch at Hinge *C*; 2, the rotary drive device of link *AB*; 3, the reducer of link *AB*; 4, the reducer of link *ED*; 5, the drive motor of link *ED*; 6, the rotary motor at output; 7, the electromagnet chuck at output; 8, the clutch at Hinge *E*; 9, the rotary frame, (b) The origin of working state, (c) The specify position, (d) The target position.

spacing was applied to the comparative analysis. The maximum calculation results are shown in Table 7. Each optimized variable of case 4 is in the range of the corresponding variable in Table 7, respectively. And the result of the objective function of this case is larger than the maximum average of the objective function in Table 7. This verifies the accuracy of the optimized results obtained by the optimization method. Then, the optimized mechanism is conditional double crank mechanism [43]. And its suitable workspace is shown in the red area in Fig.14.

Contours of θ_1 and θ_2 in the suitable workspace are shown in Fig. 15, respectively. In addition, the contour of distance distribution between points B and N in the suitable workspace is shown in Fig. 16 (a), and the contour of distribution of $k_J^{(1)}$ in the suitable workspace is presented in Fig. 16 (b). The distance between points B and N in the suitable workspace is L_8. From Fig. 16 (a), according to the constraint of the single-DOF configuration trajectory, $L_8 = 0.455$ m. In the single-DOF configuration, the mechanism is a double crank mechanism. In this case, the minimum of $k_J^{(2)}$ is 0.4132. The correspondence diagram of $k_J^{(2)}$ and $\theta_1^{(2)}$ in the suitable workspace is presented in Fig. 17.

VI. ROBOT PROTOTYPE MODEL

To fully considering the manufacture of the palletizing robot prototype, the sizes of the motors installed on the frame, sizes of the mechanism links, and interference in movements between the links, the link *HI* was designed as a bending link and the link *IBJ* was designed as an obtuse triangle link. The length of the link *BI* is 0.2 m, the length of the link *BJ* is 0.25 m, and $\angle IBJ = 2\pi/3$. Then all of the dimensional parameters are obtained.

The robot physical prototype has been made. As shown in Fig. 18, the working process of the robot is as follow: Firstly, the robots in the initial position. Secondly, the

output point F moves to the origin of working state. Hence, the robot is in the working state. For example, the output point F fast moves to the specify position by single-DOF configuration working state. Then, the robot transforms to 2-DOF configuration. The output point F reaches the target position by this working state. The prototype could operate well in its suitable workspace and the rationality of its design is verified.

VII. CONCLUSIONS

This paper described a controllable metamorphic palletizing robot that was designed with the advantages of a controllable mechanism and multiple configurations. The proposed design can achieve 2-DOF and single-DOF configurations and meet the requirements for different situations.

Its dimensional relationships, singularity and workspace were presented, followed by an evaluation of its kinematic performance in the workspace. Furthermore, the optimization method based on workspace discretization of metamorphic mechanisms was proposed on the basis of them. It was used to calculate the optimized dimensional parameters of the robot mechanism and validate by the conventional calculation approach. The robot prototype was made according to the optimal parameters, the feasibility and the practicality of its design was verified.

To ensure well operating of its palletizing processes, the analysis and experiments of the kinematic accuracy and dynamics will be the future work. The work of this paper provides a theoretical basis for the dimensional optimization of metamorphic mechanisms as well as an important reference

for the application of metamorphic mechanisms to practical engineering problems.

APPENDIX

The forward analyses of 2-DOF and single-DOF configurations are shown as follow.

In 2-DOF configuration, $\theta_1^{(1)}$ and $\theta_2^{(1)}$ are inputs, then

$$\begin{cases} \theta_3^{(1)} = (\psi_1 + \psi_2) - \pi \\ \theta_4^{(1)} = \psi_1 - \psi_3 \end{cases}$$

where

$$\begin{cases} \psi_1 = \tan^{-1}\left(\dfrac{d_1 - b_1}{c_1 - a_1}\right) \\ \psi_2 = \cos^{-1}\left(\dfrac{L_3^2 + L_{BD}^2 - L_4^2}{2L_3L_{BD}}\right) \\ \psi_3 = \cos^{-1}\left(\dfrac{L_4^2 + L_{BD}^2 - L_3^2}{2L_4L_{BD}}\right) \end{cases}$$

$$\begin{cases} a_1 = x_A + L_1\cos\theta_1^{(1)} \\ b_1 = y_A + L_1\sin\theta_1^{(1)} \\ c_1 = x_E + L_2\cos\theta_2^{(1)} \\ d_1 = y_E + L_2\sin\theta_2^{(1)} \\ L_{BD} = \sqrt{(d_1 - b_1)^2 + (c_1 - a_1)^2} \end{cases}$$

In 2-DOF configuration, only $\theta_1^{(2)}$ is input, then

$$\begin{cases} \theta_2^{(2)} = \begin{cases} \pi - \kappa + \gamma & (x_E < x_A) \cup [(x_E = x_A) \cap (y_E < y_A)] \\ \kappa + \gamma & (x_E > x_A) \cup [(x_E = x_A) \cap (y_E > y_A)] \end{cases} \\ \begin{cases} \theta_3^{(2)} = \bar{\nu} + \vartheta_1 \\ \theta_4^{(2)} = \bar{\nu} - \vartheta_2 - \pi \end{cases} \end{cases}$$

where

$$\begin{cases} \bar{\nu} = \begin{cases} \pi - \nu + \gamma & (x_E > x_A) \cup [(x_E = x_A) \cap (y_E > y_A)] \\ \nu + \gamma & (x_E < x_A) \cup [(x_E = x_A) \cap (y_E < y_A)] \end{cases} \\ \nu = 2\tan^{-1}\left(\dfrac{a_2 - \sqrt{a_2^2 + b_2^2 - c_2^2}}{b_2 - c_2}\right) \\ \kappa = 2\tan^{-1}\left(\dfrac{d_2 - \sqrt{d_2^2 + e_2^2 - f_2^2}}{e_2 - f_2}\right) \\ \vartheta_1 = \cos^{-1}\left(\dfrac{L_3^2 + L_8^2 - L_4^2}{2L_3L_8}\right) \\ \vartheta_2 = \cos^{-1}\left(\dfrac{L_8^2 + L_4^2 - L_3^2}{2L_8L_4}\right) \end{cases}$$

where

$$\begin{cases} a_2 = 2L_1L_8\sin\phi \\ b_2 = 2L_8(L_2\cos\phi - L_7) \\ c_2 = L_2^2 + L_8^2 + L_7^2 - L_1^2 - 2L_2L_7\cos\phi \\ d_2 = 2L_2L_1\sin\phi \\ e_2 = 2L_1(L_2\cos\phi - L_7) \\ f_2 = L_8^2 - L_2^2 - L_1^2 - L_7^2 + 2L_2L_7\cos\phi \\ \gamma = \tan^{-1}\left(\dfrac{y_E - y_A}{x_E - x_A}\right) \\ \phi = \begin{cases} \pi - \theta_1^{(2)} + \gamma & (x_E < x_A) \cup [(x_E = x_A) \cap (y_E < y_A)] \\ \theta_1^{(2)} - \gamma & (x_E > x_A) \cup [(x_E = x_A) \cap (y_E > y_A)] \end{cases} \end{cases}$$

Lengths of each link (including (x_A, y_A) and (x_E, y_E)) are known, as shown in Fig. 3. Then, an inverse kinematics analysis can be performed to solve for $\theta_1^{(\xi)}$, $\theta_2^{(\xi)}$, $\theta_3^{(\xi)}$ and $\theta_4^{(\xi)}$ based on known coordinate values of output F (x_F, y_F), as follows:

$$\begin{cases} \theta_1^{(\xi)} = \tan^{-1}\left(\dfrac{y_A - y_F}{x_A - x_F}\right) + \cos^{-1}\left(\dfrac{L_1^2 + L_{AF}^2 - L_6^2}{2L_1L_{AF}}\right) \\ y_B = y_A + L_1\sin\theta_1^{(\xi)} \\ x_B = x_A + L_1\cos\theta_1^{(\xi)} \\ \theta_3^{(\xi)} = \tan^{-1}\left(\dfrac{y_B - y_F}{x_B - x_F}\right) \\ y_C = y_A + L_1\sin\theta_1^{(\xi)} + L_3\sin\theta_3^{(\xi)} \\ x_C = x_A + L_1\cos\theta_1^{(\xi)} + L_3\cos\theta_3^{(\xi)} \\ \theta_2^{(\xi)} = \tan^{-1}\left(\dfrac{y_E - y_C}{x_E - x_C}\right) + \cos^{-1}\left(\dfrac{L_2^2 + L_{CF}^2 - L_4^2}{2L_2L_{CF}}\right) \\ y_D = y_E + L_2\sin\theta_2^{(\xi)} \\ x_D = x_E + L_2\cos\theta_2^{(\xi)} \\ \theta_4^{(\xi)} = \tan^{-1}\left(\dfrac{y_D - y_C}{x_D - x_C}\right) \end{cases}$$

where

$$\begin{cases} L_{AF} = \sqrt{(x_A - x_F)^2 + (y_A - y_F)^2} \\ L_{CF} = \sqrt{(x_C - x_F)^2 + (y_C - y_F)^2} \end{cases}$$

Variables ν_{12} and κ_{12} in (3) are as follows.

$$\begin{cases} \nu_{12} = 2\tan^{-1}\left(\dfrac{a_{12} - \sqrt{a_{12}^2 + b_{12}^2 - c_{12}^2}}{b_{12} - c_{12}}\right) \\ \kappa_{12} = 2\tan^{-1}\left(\dfrac{d_{12} - \sqrt{d_{12}^2 + e_{12}^2 - f_{12}^2}}{e_{12} - f_{12}}\right) \end{cases}$$

where

$$\begin{cases} a_{12} = 2L_1L_3\sin\phi \\ b_{12} = 2L_3[(L_2 \pm L_4)\cos\phi - L_7] \\ c_{12} = (L_2 \pm L_4)^2 + L_3^2 + L_7^2 - L_1^2 - 2(L_2 \pm L_4)L_7\cos\phi \\ d_{12} = 2(L_2 \pm L_4)L_1\sin\phi \\ e_{12} = 2L_1[(L_2 \pm L_4)\cos\phi - L_7] \\ f_{12} = L_3^2 - (L_2 \pm L_4)^2 - L_1^2 - L_7^2 + 2(L_2 \pm L_4)L_7\cos\phi \end{cases}$$

Variables ν_{22} and κ_{22} in (4) are as follows.

$$\begin{cases} \nu_{22} = 2\tan^{-1}\left(\dfrac{a_{22} - \sqrt{a_{22}^2 + b_{22}^2 - c_{22}^2}}{b_{22} - c_{22}}\right) \\ \kappa_{22} = 2\tan^{-1}\left(\dfrac{d_{22} - \sqrt{d_{22}^2 + e_{22}^2 - f_{22}^2}}{e_{22} - f_{22}}\right) \end{cases}$$

where

$$\begin{cases} a_{22} = 2L_1(L_4 \mp L_3)\sin\phi \\ b_{22} = 2(L_4 \mp L_3)(L_2\cos\phi - L_7) \\ c_{22} = L_2^2 + (L_4 \mp L_3)^2 + L_7^2 - L_1^2 - 2L_2L_7\cos\phi \\ d_{22} = 2L_2L_1\sin\phi \\ e_{22} = 2L_1(L_2\cos\phi - L_7) \\ f_{22} = (L_4 \mp L_3)^2 - L_2^2 - L_1^2 - L_7^2 + 2L_2L_7\cos\phi \end{cases}$$

Variables ν_{23}, κ_{23}, and δ in (6) are as follows.

$$\begin{cases} \nu_{23} = 2\tan^{-1}\left(\dfrac{a_{23} - \sqrt{a_{23}^2 + b_{23}^2 - c_{23}^2}}{b_{23} - c_{23}}\right) \\ \kappa_{23} = 2\tan^{-1}\left(\dfrac{d_{23} - \sqrt{d_{23}^2 + e_{23}^2 - f_{23}^2}}{e_{23} - f_{23}}\right) \end{cases}$$

where

$$\begin{cases} a_{23} = 2L_1L_3\sin\varphi \\ b_{23} = 2L_3(L_4\cos\varphi - L_{AD}) \\ c_{23} = L_4^2 + L_3^2 + L_{AD}^2 - L_1^2 - 2L_4L_{AD}\cos\varphi \\ d_{23} = 2L_4L_1\sin\varphi \\ e_{23} = 2L_1(L_4\cos\varphi - L_{AD}) \\ f_{23} = L_3^2 - L_4^2 - L_1^2 - L_{AD}^2 + 2L_4L_{AD}\cos\varphi \\ \delta = \tan^{-1}\left(\dfrac{y_D - y_A}{x_D - x_A}\right) \\ L_{AD} = \sqrt{(x_A - x_D)^2 + (y_A - y_D)^2} \end{cases}$$

REFERENCES

[1] J. S. Dai and J. Rees Jones, "Mobility in metamorphic mechanisms of foldable/erectable kinds," *J. Mech. Design*, vol. 121, no. 3, pp. 375–382, Sep. 1999.

[2] J. J. Parise, L. L. Howell, and S. P. Magleby, "Ortho-planar mechanisms," in *Proc. ASME Des. Eng. Tech. Conf.*, Baltimorem, MD, USA, 2000, pp. 1–10.

[3] C. Galletti and E. Giannotti, "Multiloop kinematotropic mechanisms," in *Proc. 27th Biennial Mech. Robot. Conf.*, vol. 5, Montreal, QC, Canada, 2002, pp. 455–460.

[4] D. W. Carroll, S. P. Magleby, L. L. Howell, R. H. Todd, and C. P. Lusk, "Simplified manufacturing through a metamorphic process for compliant ortho-planar mechanisms," in *Proc. Design Eng., Parts A B*, Orlando, FL, USA, Jan. 2005, pp. 389–399.

[5] I.-M. Chen, H.-S. Li, and A. Cathala, "Mechatronic design and locomotion of Amoebot—A metamorphic underwater vehicle," *J. Robotic Syst.*, vol. 20, no. 6, pp. 307–314, Jun. 2003.

[6] W. Chen, J. Zhang, J. Quan, and T. Lv, "A novel spherical joint designed for metamorphic mechanism," in *Proc. IEEE Conf. Robot., Autom. Mechatronics*, Chengdu, China, Sep. 2008, pp. 976–981.

[7] J. S. Dai, D. Wang, and L. Cui, "Orientation and workspace analysis of the multifingered metamorphic hand-metahand," *IEEE Trans. Robot.*, vol. 25, no. 4, pp. 942–947, Aug. 2009.

[8] D. Gan, J. S. Dai, and Q. Liao, "Constraint analysis on mobility change of a novel metamorphic parallel mechanism," *Mechanism Mach. Theory*, vol. 45, no. 12, pp. 1864–1876, Dec. 2010.

[9] D. Gan, J. S. Dai, J. Dias, and L. Seneviratne, "Reconfigurability and unified kinematics modeling of a 3rTPS metamorphic parallel mechanism with perpendicular constraint screws," *Robot. Comput.-Integr. Manuf.*, vol. 29, no. 4, pp. 121–128, Aug. 2013.

[10] K. Xu and X. L. Ding, "Typical gait analysis of a six-legged robot in the context of metamorphic mechanism theory," *Chin. J. Mech. Eng.*, vol. 26, no. 4, pp. 147–159, 2013.

[11] T. Wu, W. X. Zhang, and X. L. Ding, "Design and analysis of a novel parallel metamorphic mechanism," *J. Mech. Eng.*, vol. 51, no. 7, pp. 30–37, Jan. 2015.

[12] W. Ye, Y. Fang, K. Zhang, and S. Guo, "Mobility variation of a family of metamorphic parallel mechanisms with reconfigurable hybrid limbs," *Robot. Comput.-Integr. Manuf.*, vol. 41, pp. 145–162, Oct. 2016.

[13] K. Xu, L. Li, S. Bai, Q. Yang, and X. Ding, "Design and analysis of a metamorphic mechanism cell for multistage orderly deployable/retractable mechanism," *Mechanism Mach. Theory*, vol. 111, pp. 85–98, May 2017.

[14] X. Cui, J. Sun, X. Zhang, S. Xu, and J. Dai, "A metamorphic hand with coplanar reconfiguration," in *Proc. Int. Conf. Reconfigurable Mech. Robots*, Delft, The Netherlands, Jun. 2018, pp. 1–7.

[15] J. Wei and J. S. Dai, "Reconfiguration-aimed and manifold-operation based type synthesis of metamorphic parallel mechanisms with motion between 1R2T and 2R1T," *Mechanism Mach. Theory*, vol. 139, pp. 66–80, Sep. 2019.

[16] G. Jia, H. Huang, B. Li, Y. Wu, Q. Cao, and H. Guo, "Synthesis of a novel type of metamorphic mechanism module for large scale deployable grasping manipulators," *Mechanism Mach. Theory*, vol. 128, pp. 544–559, Oct. 2018.

[17] T. J. Zhao, Y. W. Wang, and M. J. Sun, "Structure design and analysis of metamorphic mobile robot based on screw theory," in *Proc. IEEE Int. Conf. Intell. Saf. Robot. (ISR)*, Shenyang, China, Aug. 2018, pp. 50–55.

[18] R. Wang, Y. Liao, J. S. Dai, H. Chen, and G. Cai, "The isomorphic design and analysis of a novel plane-space polyhedral metamorphic mechanism," *Mechanism Mach. Theory*, vol. 131, pp. 152–171, Jan. 2019.

[19] Y. Song, X. Ma, and J. S. Dai, "A novel 6R metamorphic mechanism with eight motion branches and multiple furcation points," *Mechanism Mach. Theory*, vol. 142, Dec. 2019, Art. no. 103598.

[20] W. X. Zhang, T. Wu, and X. L. Ding, "An optimization method for a novel parallel metamorphic mechanism," in *Proc. 11th World Congr. Intell. Control Autom.*, Shenyang, China, Jun. 2014, pp. 3642–3647.

[21] W. Zhang, T. Wu, and X. Ding, "An optimization method for metamorphic mechanisms based on multidisciplinary design optimization," *Chin. J. Aeronaut.*, vol. 27, no. 6, pp. 1612–1618, Dec. 2014.

[22] D. Chablat and P. Wenger, "Architecture optimization of a 3-DOF translational parallel mechanism for machining applications, the orthoglide," *IEEE Trans. Robot. Autom.*, vol. 19, no. 3, pp. 403–410, Jun. 2003.

[23] M. Zoppi, D. Zlatanov, and C. M. Gosselin, "Analytical kinematics models and special geometries of a class of 4-DOF parallel mechanisms," *IEEE Trans. Robot.*, vol. 21, no. 6, pp. 1046–1055, Dec. 2005.

[24] C. Menon, R. Vertechy, M. C. Markot, and V. Parenti-Castelli, "Geometrical optimization of parallel mechanisms based on natural frequency evaluation: Application to a spherical mechanism for future space applications," *IEEE Trans. Robot.*, vol. 25, no. 1, pp. 12–24, Feb. 2009.

[25] R. Wang and X. Zhang, "Parameters optimization and experiment of a planar parallel 3-DOF nanopositioning system," *IEEE Trans. Ind. Electron.*, vol. 65, no. 3, pp. 2388–2397, Mar. 2018.

[26] T. Sun, B. Lian, J. Zhang, and Y. Song, "Kinematic calibration of a 2-DoF over-constrained parallel mechanism using real inverse kinematics," *IEEE Access*, vol. 6, pp. 67752–67761, Dec. 2018.

[27] T. Sun, B. Lian, Y. Song, and L. Feng, "Elastodynamic optimization of a 5-DoF parallel kinematic machine considering parameter uncertainty," *IEEE/ASME Trans. Mechatronics*, vol. 24, no. 1, pp. 315–325, Feb. 2019.

[28] S. Erkaya, "Trajectory optimization of a walking mechanism having revolute joints with clearance using ANFIS approach," *Nonlinear Dyn.*, vol. 71, nos. 1–2, pp. 75–91, Jan. 2013.

[29] Y. Zhao, G. Chen, H. Wang, and Z. Lin, "Optimum selection of mechanism type for heavy manipulators based on particle swarm optimization method," *Chin. J. Mech. Eng.*, vol. 26, no. 4, pp. 763–770, 2013.

[30] A. Karimi, M. T. Masouleh, and P. Cardou, "Avoiding the singularities of 3-RPR parallel mechanisms via dimensional synthesis and self-reconfigurability," *Mechanism Mach. Theory*, vol. 99, pp. 189–206, May 2016.

[31] R. M. C. Rayner, M. N. Sahinkaya, and B. Hicks, "Improving the design of high speed mechanisms through multi-level kinematic synthesis, dynamic optimization and velocity profiling," *Mechanism Mach. Theory*, vol. 118, pp. 100–114, Dec. 2017.
[32] S. Briot and A. Goldsztejn, "Topology optimization of industrial robots: Application to a five-bar mechanism," *Mechanism Mach. Theory*, vol. 120, pp. 30–56, Feb. 2018.
[33] D.-S. Zhang, Y.-D. Xu, J.-T. Yao, and Y.-S. Zhao, "Analysis and optimization of a spatial parallel mechanism for a new 5-DOF hybrid serial-parallel manipulator," *Chin. J. Mech. Eng.*, vol. 31, no. 1, pp. 1–9, Dec. 2018.
[34] Y. Liang, L. Sun, Z. Du, Z. Yan, and W. Wang, "Mechanism design and optimization of a haptic master manipulator for laparoscopic surgical robots," *IEEE Access*, vol. 7, pp. 147808–147824, Oct. 2019.
[35] J. H. Lee and J. H. Park, "Optimization of postural transition scheme for quadruped robots trotting on various surfaces," *IEEE Access*, vol. 7, pp. 168126–168140. Dec. 2019.
[36] G. Park, J. Hong, S. Yoo, H. S. Kim, and T. Seo, "Design of a 3-DOF parallel manipulator to compensate for disturbances in facade cleaning," *IEEE Access*, vol. 8, pp. 9015–9022, Jan. 2020.
[37] T. Zhang, C. L. P. Chen, L. Chen, X. Xu, and B. Hu, "Design of highly nonlinear substitution boxes based on I-Ching operators," *IEEE Trans. Cybern.*, vol. 48, no. 12, pp. 3349–3358, Dec. 2018.
[38] T. Zhang, G. Su, C. Qing, X. Xu, B. Cai, and X. Xing, "Hierarchical lifelong learning by sharing representations and integrating hypothesis," *IEEE Trans. Syst., Man, Cybern. Syst.*, early access, Feb. 27, 2019, doi: 10.1109/TSMC.2018.2884996.
[39] T. Zhang, X. Wang, X. Xu, and C. L. P. Chen, "GCB-Net: Graph convolutional broad network and its application in emotion recognition," *IEEE Trans. Affect. Comput.*, vol. 14, no. 8, pp. 1–10. Jul. 2019.
[40] D. Gan, J. S. Dai, and Q. Liao, "Mobility change in two types of metamorphic parallel mechanisms," *J. Mech. Robot.*, vol. 1, no. 4, Nov. 2009, Art. no. 041007.
[41] D. L. Li, Z. H. Zhang, J. S. Dai, and K. T. Zhang, "Overview and prospects of metamorphic mechanism," *J. Mech. Eng.*, vol. 46, no. 13, pp. 14–21, Jul. 2010.
[42] K.-L. Ting and Y.-W. Liu, "Rotatability laws for N-bar kinematic chains and their proof," *J. Mech. Design*, vol. 113, no. 1, pp. 32–39, Mar. 1991.
[43] H. Li, "Fundamental Study on the hybrid-driven programmable mechanical press," Ph.D. dissertation, Dept. Mech. Eng., Tianjin Univ., Tianjing, China, 2003.
[44] G. Feng, Z. Xiao-Qiu, Z. Yong-Sheng, and Z. Wen-Buo, "Distribution of some properties in physical model of the solution space of 2-DOF parallel planar manipulators," *Mechanism Mach. Theory*, vol. 30, no. 6, pp. 811–817, Aug. 1995.
[45] J. K. Salisbury and J. J. Craig, "Articulated hands: Force control and kinematic issues," *Int. J. Robot. Res.*, vol. 1, no. 1, pp. 4–17, Mar. 1982.
[46] T. Yoshikawa, "Dynamic manipulability of robot manipulators," in *Proc. IEEE Int. Conf. Robot. Autom.*, St. Louis, MO, USA, Mar. 1985, pp. 1033–1038.

HUIQING CHEN received the B.S. degree from the Kunming University of Science and Technology, in 2012, and the M.S. degree from Guangxi University, in 2015, where he is currently pursuing the Ph.D. degree. His research interests include robotic mechanisms, mechanical dynamics, and nonlinear vibration theory.

NINGQI ZHOU received the B.S. degree from the Southwest University of Science and Technology, in 2018. She is currently pursuing the M.S. degree with Guangxi University. Her research interests include robotic mechanisms, mechanical dynamics, and reliability engineering.

RUGUI WANG (Member, IEEE) received the Ph.D. degree from Guangxi University, China, in 2008. From 2015 to 2016, he was a Visiting Scholar with the Centre for Robotics Research, King's College London, University of London, London, U.K. He is currently a Professor with Guangxi University and a Visiting Scholar with Tsinghua University, China. His research interests include robotic mechanisms, metamorphic mechanism, reconfigurable mechanisms, and design of robots.